Applied Physics B (2018) 124:138
https://doi.org/10.1007/s00340-018-7003-0

Applied Physics B
Lasers and Optics

Fabry–Perot etalon-based ultraviolet high-spectral-resolution lidar for tropospheric temperature and aerosol measurement

Fahua Shen[1] · Peng Zhuang[2] · Wenjuan Shi[1] · Chengqun Qiu[1] · Bangxin Wang[2] · Chenbo Xie[2]

Received: 31 December 2017 / Accepted: 5 June 2018 / Published online: 19 June 2018

Abstract

The 355-nm ultraviolet high-spectral-resolution technique based on a triple Fabry–Perot etalon (FPE) for simultaneous high-accuracy measurement of tropospheric temperature and aerosol is proposed. The detection principle is analyzed and the whole structure of lidar system is designed. The parameters of the triple FPE-labeled FPE-1, FPE-2 and FPE-L are optimized in detail. FPE-1, FPE-2 and FPE-L are used for measuring aerosol and separating Rayleigh signal from Mie signal, for measuring temperature and for frequency locking, respectively. The performance simulation of the proposed lidar system showed that the measurement errors of temperature and backscatter ratio are below 2 K and 0.17% at 8 km and below 4 K and 0.39% at 12 km with 30-m range resolution and 1-min integration time using a 48 mJ pulse energy and 20 Hz repetition rate laser and a 25-cm telescope. The influence of Mie signal contamination on temperature measurement mainly depends on the relative Mie rejection factors of the two channels for temperature measurement, which are 4.2 and 10.4% of our proposed system at 270 K and the corresponding temperature deviation is 1 K with backscatter ratio of 10 and Rayleigh photoelectrons of 10^5. Assuming the same number of total photoelectrons received, the backscatter ratio and temperature measurement accuracies of our proposed lidar are 4.16–22.58 and 2.07–2.76 times, respectively, that of the traditional dual-pass multi-cavity-FPE-based HSRL at temperature of 220–290 K and backscatter ratio of 1–10.

1 Introduction

Atmospheric temperature and aerosol optical properties are both extremely important atmospheric parameters. The detection data of atmospheric temperature and aerosol optical properties with high accuracy and high temporal and spatial resolution have important applications in atmospheric scientific research, weather forecasting, climate change analysis, environmental monitoring and so on. At present, there are mainly three kinds of lidar for aerosol detection: Mie lidar [1–3], polarization lidar [4, 5] and high-spectral-resolution lidar (HSRL) [6, 7]. Because the backscattering signal contains the information of two atmospheric parameters, that is the scattering coefficient and the extinction coefficient, some assumptions need to be made about the atmospheric state during the inversion process of Mie lidar [1, 2], such as the assumption of the lidar ratio [2]. However, the assumed parameter values often deviate from the true values, resulting in large deviations of the inversion results [3]. When using the lidar equation to retrieve the aerosol extinction coefficient, the polarization lidar still needs to do the same hypothesis as dealing with the Mie lidar equation [4, 5]. The HSRL separates Mie signal and Rayleigh signal from the total atmospheric backscattering signal using high-spectral-resolution interferometer, the atomic or molecular absorption filter. Therefore, the extinction coefficient can be directly derived without any assumptions, improving the accuracy of parameter inversion [6, 7]. However, through in-depth analysis, it is found that the atmospheric temperature is still needed to deduct the Rayleigh scattering signal in the exact inversion. At present, there are mainly four methods for atmospheric temperature measurement: differential absorption method [8–11], Rayleigh scattering integral method [12–14], Rayleigh scattering spectroscopy (i.e. HSRL technique) [15–27] and rotational Raman scattering method [14, 28–33]. The differential absorption method has high

✉ Fahua Shen
shenfh@yctu.edu.cn

[1] Department of New Energy and Electronic Engineering, Yancheng Teachers University, 2 Hope Avenue South Road, Yancheng 224007, Jiangsu, China

[2] Anhui Institute of Optics and Fine Mechanics, Key Laboratory of Atmospheric Optics, Chinese Academy of Sciences, 350 Shushanghu Road, Hefei 230031, Anhui, China

requirements on the monochromaticity of laser, and at least two wavelengths should be used [10]. At the same time, the concentration of the measured gas needs to be stable, which is generally difficult to achieve. Therefore, the system has low measurement accuracy, complex structure and high cost. The Rayleigh scattering integral method directly detects the atmospheric density, and then obtains the atmospheric temperature distribution through the gas equation of state. But the aerosol contamination and ozone absorption make the lidar backscatter signal no longer proportional to the molecular number density in the troposphere and lower stratosphere. Therefore, this method is only suitable for measuring the middle atmosphere above 30 km [3, 13]. The HSRL techniques measure the atmospheric temperature using the full width half maximum (FWHM) of Rayleigh scattering spectrum as a function of temperature, and then a high-performance spectrometer, such as interferometers [15–17, 22–25], atomic vapor, or molecular vapor absorption filters [21, 26], should be used to detect the spectral information. They can be divided into two categories according to different implementations. One is to obtain the entire backscattered spectrum line by scanning the Fabry–Perot interferometer or laser frequency, and to get the FWHM of spectrum by nonlinear fitting method [15, 16, 25]; the other is to detect the temperature sensitive parts of the backscattered spectrum line using static filters, and to obtain temperature using the relationship between the detection signals and the temperature [17–24, 26, 27]. However, the detection accuracy of low-altitude atmospheric temperature is seriously affected by strong aerosol contamination. The HSRL techniques of measuring the FWHM of atmospheric Rayleigh–Brillouin scattering spectrum to detect the temperature in low-altitude atmosphere can reduce the effect of Mie scattering in the frequency domain and improve the measurement accuracy. However, since there is only an approximate relationship in theory between the FWHM of Rayleigh–Brillouin scattering spectrum and temperature, the temperature measurement accuracy is not high, about 5 K [27]. In addition, Raman lidar can be used to detect low-altitude atmospheric temperatures from 0 to 11 km. Nevertheless, the intensity of Raman scattering signals is weaker 3–4 orders of magnitude than that of Mie and Rayleigh scattering, so to achieve accurate measurement, it requires high power laser, large aperture receiving telescope and high-precision and high-efficiency optical spectroscope, resulting in high cost and a very limited range of application [31].

To solve the dilemma of low-altitude atmospheric temperature detection, Prof. Hua et al. proposed a kind of ultraviolet (UV) Rayleigh–Mie lidar for accurate temperature measurement in troposphere in 2005 [23]. The lidar uses a multi-channel FPE, the transmission spectrum center of one channel etalon is located near the central frequency of the backscatter spectrum for aerosol measurement; the single-order transmission spectrum centers of the other two channel etalons are located at different locations on one side of the backscatter spectrum for temperature measurement, and the backscattered light is passed through the two-channel etalons twice in succession to suppress aerosol scattering signal. Mie correction is applied in the temperature inversion process, achieving simultaneous detection of temperature and aerosols with good accuracy [24]. Based on this, we propose an ultraviolet triple FPE-based HSRL technique, which can simultaneously detect the tropospheric temperature and aerosol with high accuracy. The three channels of the triple FPE are aerosol channel, temperature channel and locking channel. The polarization isolation technique is used to improve the utilization of lidar echo signal and effectively suppress the solar background noise. By optimizing the free spectral spacing (FSR) of FPE, two adjacent orders of the temperature channel etalon spectrum can be used for simultaneous measuring of the two wings of the Rayleigh backscattering spectrum, and then obtain a higher SNR for temperature detection. By optimizing the plate reflectivities of temperature channel and aerosol channel etalons, the temperature and backscatter ratio detection sensitivities can both reach high values, and the simultaneous detection of temperature and aerosol can be achieved.

2 Measurement principle

The principle of tropospheric temperature and aerosol measurement with FPE-based high-spectral-resolution technique is shown in Fig. 1. A triple etalon is adopted whose three channels are aerosol channel etalon (FPE-1), temperature channel etalon (FPE-2) and locking channel etalon (FPE-L). The peak of the FPE-L spectrum is located half-width

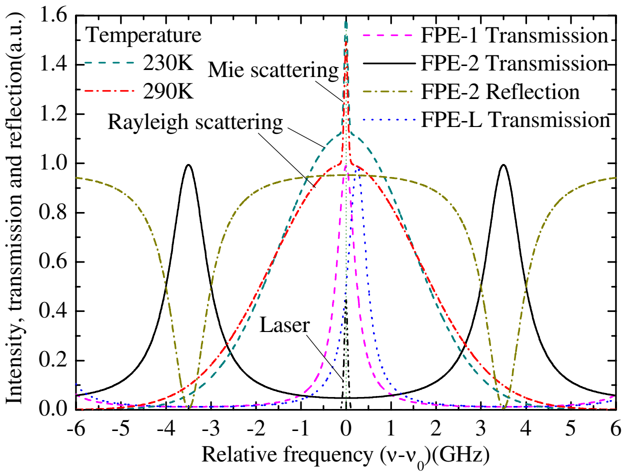

Fig. 1 The principle of temperature and aerosol measurement with FPE-based high-spectral-resolution technique

half-maximum of FPE-L spectrum from the peak of the FPE-1 spectrum, so the FPE-1 peak is aligned to the half-height point of the FPE-L bandpass. Actively locking the laser and the triple FPE at this point on the FPE-L ensures maximum spectral discrimination ratio of FPE-1 and minimum aerosol and wind speed measurement error. We accomplish the locking by sampling a small portion of the transmitted laser energy to make a reference measurement of the outgoing frequency. The reference signal transmitted through the FPE-L is detected and divided by the total energy of the incident reference signal to obtain transmittance value, which can be used to measure the outgoing laser frequency providing correction for short-term frequency jitter and lock the triple FPE (all three channels together) to the laser frequency using the pre-calibrated curve of FPE-L transmittance. The optical paths of FPE-1 and FPE-2 are designed in cascade, which can improve the detection SNR. The atmospheric backscattering light first passes through FPE-1, transmitting most of the aerosol scattering light and a small amount of molecular scattering light, reflecting most of the molecular scattering light and a very small amount of aerosol scattering light. Then, the backscatter ratio can be obtained using the transmitted and reflected signals of FPE-1. Most of the molecular scattering light reflected by FPE-1 passes through FPE-2. Due to the molecular scattering spectra at different atmospheric temperatures being different, the transmitted and reflected signals at different temperatures passing through FPE-2 are different. Then, the atmospheric temperature information can be obtained using the ratio of the transmitted and reflected signals of FPE-2.

3 The structure of FPE-based HSRL system

The structure of the UV FPE-based HSRL for measuring tropospheric temperature and aerosol is illustrated in Fig. 2. A seed injection Nd:YAG laser is used as the emission source, and the 355-nm linearly polarized laser beam is emitted after the triple frequency crystal. The emitted laser is split into two beams by the beam splitter (BS)-1 whose transmittance/reflectance ratio (*T*/*R*) is 99/1. After being expanded by the beam expander, the transmitted beam vertically enters the measured area of the atmosphere. The atmospheric backscattered light received by the telescope first, and then filtered by the interference filter (IF), delayed by the electro-optical modulator (EOM), limited telescope receiving field of view by the field stop, collimated by the collimation system. The collimated beam passes through the half-wave plate (HWP) to adjust the polarization direction, making it consistent with the transmission direction of the PBS behind (parallel to the paper). The collimated light beam from the HWP is normal incident on FPE-1 after passing through polarization beam splitter (PBS) and quarter-wave plate (QWP)-1. The transmission beam is received by the photomultiplier tube 1 in photon-counting mode (PMT-PC1). The reflection beam passes through QWP-1

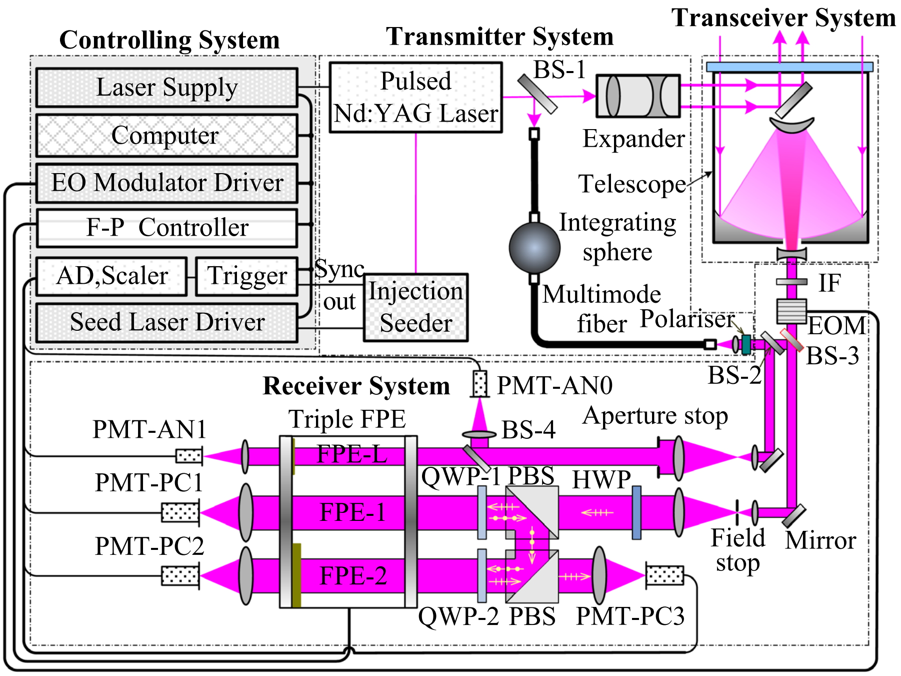

QWP: quater-wave plate HWP: half-wave plate PBS: polarization beam splitter
EOM: electro-optical modulator PMT-AN: photomultiplier tube in analog mode
IF: interference filter PMT-PC: photomultiplier tube in photon counting mode

Fig. 2 The structure of ultraviolet Fabry–Perot etalon-based HSRL again and its polarization direction becomes perpendicular to the paper. So it would be reflected by the PBS and normal incident on FPE-2 after passing through QWP-2. The transmission beam is received by the PMT-PC2. The reflection beam passes through QWP-2 again and its polarization direction becomes parallel to the paper again. So it is transmitted through PBS and then received by the PMT-PC3. The reflected beam from BS-1 is coupled into the integrating sphere by the multimode fiber. The integrating sphere spreads the pulsed laser light into continuous light as the reference. The polarization direction of the polarizer is the same as that of the light received by the telescope. The beam from the polarizer is split into two beams by the BS-2. The transmitted beam is reflected by the BS-3, and then enters the same optical path as the atmospheric backscattering light. It is used for the calibration measurements of the FPE-1 and FPE-2 spectra, and is isolated from the backscattering light in time sequence. After being collimated by the collimation system and compressed by the aperture stop, the reflected beam of BS-2 is split into two beams by BS-4. The reflected beam is received by the photomultiplier tube 0 in analog mode (PMT-AN0). The transmitted beam is normal incident on FPE-L and received by PMT-AN1. The output signals of two analog detectors and three photon-counting detectors are collected by A/D card and photon-counting acquisition card, respectively, and then processed, stored, retrieved and displayed by an industry programmable computer (IPC). The whole system's laser, FPE, EOM drive, A/D and photon-counting acquisition card, etc. are controlled by the IPC through the RS232 interface.

4 Optimization of the triple FPE's parameters

Assume that the Mie- and Rayleigh-backscattering spectra are Gaussian distribution, the transmittances of the Mie- and Rayleigh-backscattering light with a center frequency of ν_{s} being incident on FPE-1, incident on FPE-2 after reflecting by FPE-1, reflected by FPE-2 after reflecting by FPE-1 are, respectively,

$$T_{1x}(\nu_{\mathrm{s}}) = \int_{-\infty}^{\infty} f_x(\nu - \nu_{\mathrm{s}}) h_1(\nu - \nu_1) \mathrm{d}\nu \tag{1}$$

$$T_{2x}(\nu_{\mathrm{s}}) = \int_{-\infty}^{\infty} f_x(\nu - \nu_{\mathrm{s}}) [C - \mu_1 h_1(\nu - \nu_1)] h_2(\nu - \nu_2) \mathrm{d}\nu \tag{2}$$

$$T_{3x}(\nu_{\mathrm{s}}) = \int_{-\infty}^{\infty} f_x(\nu - \nu_{\mathrm{s}}) [C - \mu_1 h_1(\nu - \nu_1)] [C - \mu_2 h_2(\nu - \nu_2)] \mathrm{d}\nu, \tag{3}$$

where $x = a, m$, which, respectively, represents aerosol Mie scattering (or outgoing laser) and molecular Rayleigh scattering; h_i is the transmission function for FPE-i $(i = 1, 2)$; ν_i is the central frequency of FPE-i; $C = 1 - A$, A is the loss coefficient accounting for any absorptive or scattering losses in the FPE-i plates; $\mu_i = (1 - R_i C)/(C - R_i)$, R_i is the plate reflectivity of FPE-i; f_a and f_m are the normalized Gaussian Mie- and Rayleigh-scattering spectral functions, respectively. The spectral distribution of molecular scattering can be more accurately estimated from a Rayleigh–Brillouin theory based on S6 model [34]. The Gaussian distribution used here is an appropriate approximation of Rayleigh scattering for theoretical analysis. The loss of FPEs is carefully considered in the above equations. After solving the above integral formula, we obtain

$$T_{1x}(\nu_{\mathrm{s}}) = \eta_1 (1 + 2\sigma_{1x}) \tag{4}$$

$$T_{2x}(\nu_{\mathrm{s}}) = C\eta_2 (1 + 2\sigma_{2x}) - \mu_1 \eta_1 \eta_2 [1 + 2(\sigma_{1x} + \sigma_{2x} + \sigma_{12x}^{+} + \sigma_{12x}^{-})] \tag{5}$$

$$T_{3x}(\nu_{\mathrm{s}}) = C^2 - C\mu_1 T_{1x}(\nu_{\mathrm{s}}) - \mu_2 T_{2x}(\nu_{\mathrm{s}}), \tag{6}$$

where

$$\sigma_{ix} = \sum_{m=1}^{\infty} R_i^m \cos\left[\frac{2\pi m(\nu_{\mathrm{s}} - \nu_i)}{\bar{\nu}_{\mathrm{FSR}}}\right] \exp\left[-\left(\frac{\pi m \Delta\nu_x}{\bar{\nu}_{\mathrm{FSR}}}\right)^2\right] \sin c\left[\frac{2m(\nu_{\mathrm{s}} - \nu_i)}{\bar{\nu}_{\mathrm{FSR}}} \frac{1 - \cos\theta_0}{1 + \cos\theta_0}\right]$$

$$\sigma_{12x}^{\pm} = \sum_{n=1}^{\infty} \sum_{m=1}^{\infty} R_1^n R_2^m \cos\left[\frac{2\pi[(n \pm m)\nu_{\mathrm{s}} - (n\nu_1 \pm m\nu_2)]}{\bar{\nu}_{\mathrm{FSR}}}\right] \times \exp\left[-\left(\frac{\pi(n \pm m)\Delta\nu_x}{\bar{\nu}_{\mathrm{FSR}}}\right)^2\right] \times \sin c\left[\frac{2[(n \pm m)\nu_{\mathrm{s}} - (n\nu_1 \pm m\nu_2)]}{\bar{\nu}_{\mathrm{FSR}}} \frac{1 - \cos\theta_0}{1 + \cos\theta_0}\right],$$

where $\nu_{\mathrm{s}} = \nu_0 \pm 2V_{\mathrm{r}}/\lambda$, λ_0 is the central frequency of emission laser, V_{r} is the vertical wind speed (generally small), λ is the laser wavelength, and θ_0 is the half divergence angle of the beam incident to FPE; $\eta_i = T_{\mathrm{p},i}(1 - R_i)/(1 + R_i)$ is the average transmittance of FPE-i, $T_{\mathrm{p},i}$ is the peak transmittance of FPE-i; $\bar{\nu}_{\mathrm{FSR}} = 2\nu_{\mathrm{FSR}}/(1 + \cos\theta_0)$, ν_{FSR} is the FSR of FPE; $\Delta\nu_a = [(\Delta\nu_l)^2 + (\Delta\nu_d)^2]^{1/2}$ is an equivalent $1/e$ linewidth of emission laser, which takes into account the spectral broadening effects caused by the finite spectra width of illumination, the surface defects and parallelism errors of FPE [35, 36]; $\Delta\nu_l = \Delta\nu/(4\ln 2)^{1/2}$, δ_ν is linewidth of actual emission laser spectrum; $\Delta\nu_d = (2\mathrm{FSR}/\lambda)[(\Delta d_D)^2 + (\alpha\rho)^2/2]^{1/2}$ is the amount of the equivalent spectrum broadening due to surface defects and parallelism errors of FPE, Δd_D is the defect factor of flatness, α is the wedge angle, and ρ is the half aperture of FPE [36]; $\Delta\nu_m^2 = \Delta\nu_a^2 + \nu_r^2, \Delta\nu_r = (8kT/M\Delta^2)^{1/2}$

is the $1/e$ width of the atmospheric molecular spectrum, k is the Boltzmann constant, T is atmospheric temperature, and M is the average mass of an atmospheric molecule. So, T_{1m}, T_{2m} and T_{3m} are also functions of temperature. The upper equations also take into account the influence of the angular dispersion of illumination, which is mainly reflected in the sin c term [35, 36]. In many literatures, the spectral broadening of imperfect FPE under non-ideal incident conditions was studied and the definition of effective finesse was put forward [35, 37, 38]. The definition of equivalent linewidth of laser proposed here is essentially the same as it.

As can be seen from Fig. 2, the number of backscattered photoelectrons received by the photon-counting detectors PMT-PC-j for $j = 1$, 2 and 3 are

$$N_j(z, \nu_s, T) = N_a(z)T_{ja}(\nu_s) + N_m(z)T_{jm}(\nu_s, T), \tag{7}$$

simultaneously. According to the error transfer formula, the measurement errors of R_β and T are, respectively,

$$\varepsilon_R = \frac{\sqrt{\theta_{RT}^2 \mathrm{SNR}_T^{-2} + \theta_T^2 \mathrm{SNR}_R^{-2}}}{\left|\theta_{RT}\theta_{TR} - \theta_R\theta_T\right|} \tag{10}$$

$$\varepsilon_T = \frac{\sqrt{\theta_R^2 \mathrm{SNR}_T^{-2} + \theta_{TR}^2 \mathrm{SNR}_R^{-2}}}{\left|\theta_{RT}\theta_{TR} - \theta_R\theta_T\right|}, \tag{11}$$

where $\theta_R = (1/S_R)\partial S_R/\partial R_\beta$ and $\theta_T = (1/S_T)\partial S_T/\partial T$ are the backscatter ratio sensitivity of S_R and the temperature sensitivity of S_T; $\theta_{RT} = (1/S_R)\partial S_R/\partial T$ and $\theta_{TR} = (1/S_T)\partial S_T/\partial R_\beta$ are the temperature sensitivity of S_R and the backscatter ratio sensitivity of S_T (cross-correlation sensitivities); SNR_R and SNR_T are the SNR for measurement of S_R and S_T, respectively, that is

$$\mathrm{SNR}_R = \left[\frac{N_1 + \eta_1 N_b/2 + N_d}{N_1^2} + \frac{N_2 + N_3 + (C - \mu_1\eta_1)(C - \mu_2\eta_2 + \eta_2)N_b/2 + 2N_d}{(N_2 + N_3)^2}\right]^{-1/2} \tag{12}$$

$$\mathrm{SNR}_T = \left[\frac{N_2 + (C - \mu_1\eta_1)\eta_2 N_b/2 + N_d}{N_2^2} + \frac{N_3 + (C - \mu_1\eta_1)(C - \mu_2\eta_2)N_b/2 + N_d}{N_3^2}\right]^{-1/2}, \tag{13}$$

where $N_a(z)$ and $N_m(z)$ are the number of photoelectrons for Mie- and Rayleigh-backscattering at altitude z received by lidar, respectively, that can be derived from lidar equations. According to the principle analysis of Sect. 2, the backscatter ratio response function and the temperature response function can be defined, respectively,

$$\begin{aligned} S_R &= \frac{N_1(z, \nu_s, T)}{N_2(z, \nu_s, T) + N_3(z, \nu_s, T)} \\ &= \frac{(R_\beta - 1)T_{1a}(\nu_s) + T_{1m}(\nu_s, T)}{(R_\beta - 1)[T_{2a}(\nu_s) + T_{3a}(\nu_s)] + [T_{2m}(\nu_s) + T_{3m}(\nu_s)]} \end{aligned} \tag{8}$$

$$S_T = \frac{N_2(z, \nu_s, T)}{N_3(z, \nu_s, T)} = \frac{(R_\beta - 1)T_{2a}(\nu_s) + T_{2m}(\nu_s, T)}{(R_\beta - 1)T_{3a}(\nu_s) + T_{3m}(\nu_s, T)}, \tag{9}$$

where $R_\beta = (\beta_a + \beta_m)/\beta_m$ is the backscatter ratio. Thus, it can be seen that both S_R and S_T are functions of R_β, T and ν_s. Because the vertical wind speed is generally very small, which is generally not more than 1 m/s in the low troposphere [39] and not more than several cm/s in the high troposphere and stratosphere [40], $\nu_s \approx \nu_0$. Then, combining Eqs. (8, 9) and using the nonlinear iterative method, the backscatter ratio and temperature can be retrieved

where N_b are the photoelectrons received by the detector for the solar background; N_d are the dark counts generated by detector itself. The background item is divided by 2 due to the background natural light passing through the polarized prism.

4.1 Preliminary optimization

It is assumed that the linewidth of the emission laser spectrum is $\delta\nu = 80$ MHz, the defect factor of flatness $\Delta d_D = 3$ nm, the wedge angle can be made negligibly small through the use of PZT elements [38] and let $\alpha = 0.1$ μrad, the aperture of FPE $2\rho = 25$ mm, the half divergence angle of the light beam incident on FPE is 0.5 mrad and the total number of incident photoelectrons is 10^5.

Assume the aerosol is measured by a single FPE which corresponds to FPE-1 of the triple FPE, and the peak of the FPE's spectrum is located in the center of the backscatter spectrum. Regardless of the effect of temperature uncertainty, the temperature is set to 270 K. Then, when the backscatter ratio is 1.1, 5 and 10, the contour plots of the backscatter ratio measurement error varying with FSR and plate reflectivity of FPE is shown in Fig. 3a–c. From Fig. 3, we can see that the measurement error of the backscatter

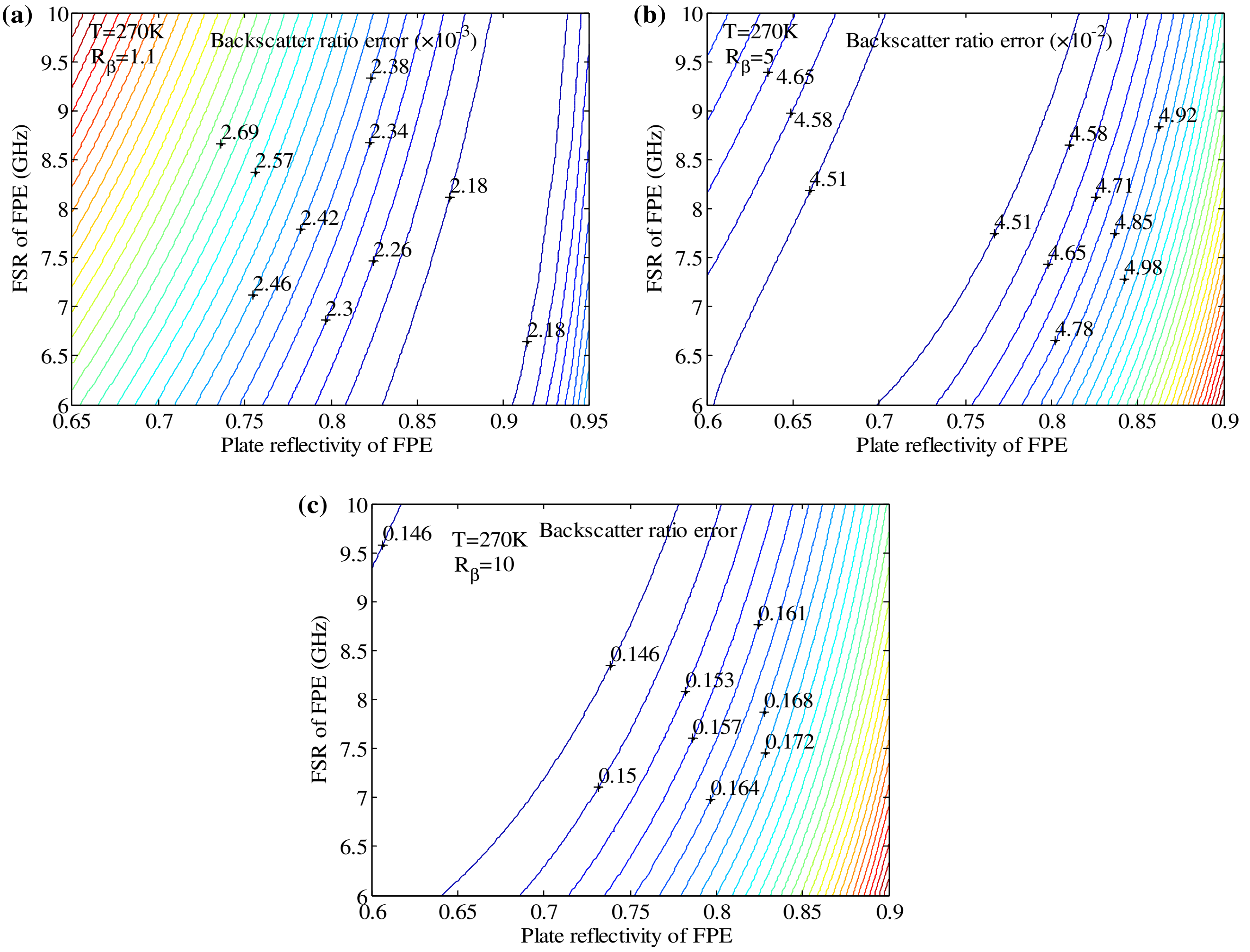

Fig. 3 When R_β is 1.1, 5 and 10, the measurement error of R_β varies with FSR and plate reflectivity of FPE

ratio mainly depends on the reflectivity of the FPE, and the optimal reflectivity is related to the magnitude of the backscatter ratio. The larger the backscatter ratio, the smaller the optimal plate reflectivity. When the backscatter ratio is 1.1, 5 and 10, the optimal plate reflectivity of FPE is 0.89, 0.72 and 0.66, respectively. Large FSR of the FPE is more favorable, which can avoid the interference of adjacent spectrum. But when the FSR is above 7 GHz, it will have little effect on the measurement error of the backscatter ratio. According to the aerosol measurement principle and Eq. (8) described above, we can see that the aerosol measurement method proposed here is similar to the single FPE-based method using FPE-1. Therefore, the optimization result of the single FPE parameter here can be considered as the optimization result of the FPE-1 parameter.

Assume the atmospheric temperature is measured using a single-order spectrum of a single FPE which corresponds to FPE-2 of the triple FPE. The influence of aerosol signal is not taken into account, the FSR of FPE is set to 12 GHz (larger values can also be ok without affecting the optimization result) and the temperature is set to 270 K. Then, the temperature measurement error varies with the reflectivity of FPE when the laser-FPE offset (the separation of the outgoing laser central frequency and the FPE central frequency) is zero which is shown in Fig. 4a; the contour plots of the temperature measurement error varying with the laser-FPE offset and the plate reflectivity of FPE are shown in Fig. 4b. From Fig. 4, we can see that there are two sets of values that can make the temperature measurement error tend to a minimum. One set is that the laser-FPE offset is zero and the plate reflectivity of FPE is 0.65–0.75, the other set is that the laser-FPE offset is 3.43 GHz and the plate reflectivity of FPE is 0.8. But the temperature detection performance is seriously affected by aerosols when the former set is used, so it is not suitable to be adopted for temperature measurement in the area with larger aerosol concentration. According to the temperature measurement principle and Eq. (9) described above, we can see that the temperature measurement method

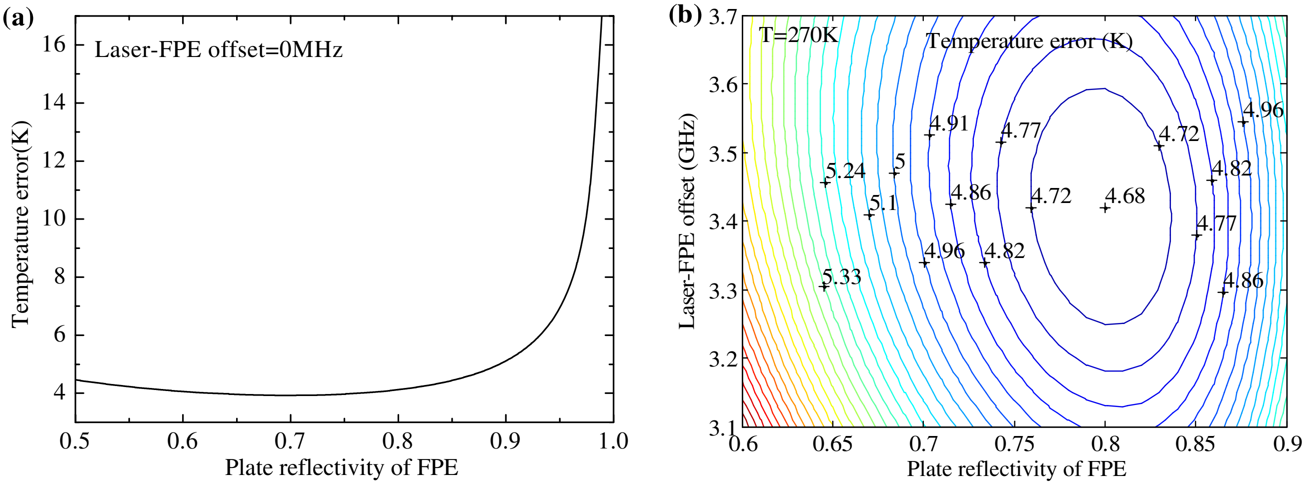

Fig. 4 The measurement error of T varies with laser-FPE offset and plate reflectivity of FPE

proposed here adopts FPE-1 and FPE-2 cascade detection mode, which is different from the single FPE-based method using FPE-2. Therefore, the actual parameter value of FPE-2 used in our triple-FPE-based system would be different from the optimization results here. However, we can foresee the following two points: one is that the optimal plate reflectivity of FPE-2 would be smaller than 0.8 due to the cascaded optical path; the other is that the optimal FSR of the FPE-2 used in our triple FPE-based system would be about twice the laser-FPE offset, that is about $3.43 \times 2 = 6.86$–7 GHz.

Based on the above optimization results, the optimal FSR of the triple FPE is about 7 GHz and the optimal plate reflectivity of FPE-1 is set to 0.75 since its optimum value is from 0.89 to 0.66 for the backscatter ratio range of 1.1–10 after considering the large aerosol concentration in low altitude and the requirement of temperature measurement. Furthermore, FPE-L is mainly for frequency locking. Under the premise of ensuring the accuracy of locking, to facilitate the triple FPE processing, FPE-1 and FPE-L are coated with the same reflective film, that is the plate reflectivity of FPE-L is also 0.75. The final linewidths of FPE-1 and FPE-L transmission spectrums are both about 720 MHz, so the peak to peak spacing of FPE-1 and FPE-L is set to 360 MHz.

4.2 Further optimization

Only considering the signal shot noise, the parameters of the triple FPE can be more carefully optimized by Eqs. (1–12). Using the same parameter values as assumed in Sect. 4.1, the contour plots that the measurement errors of backscatter ratio and temperature vary with plate reflectivity of FPE-2 and FSR of the triple FPE (since it is an integrated triple FPE, the FSR of FPE-2 is just the FSR of the triple FPE.) with the backscatter ratio of 1.1, 5 and 10 are shown in

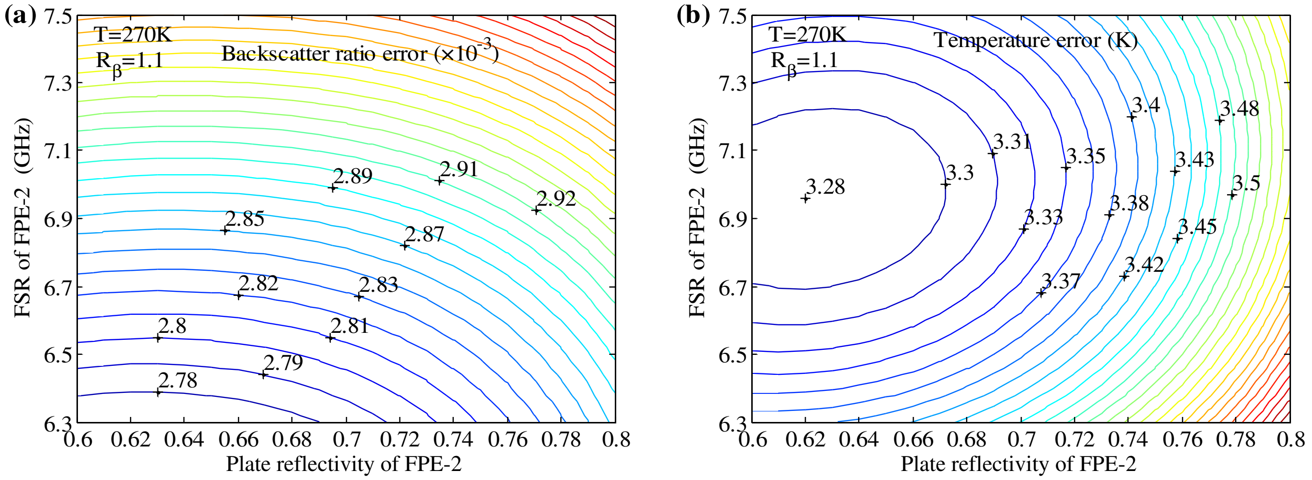

Fig. 5 When $R_\beta = 1.1$, the measurement error of R_β and T varies with plate reflectivity of FPE-2 and FSR of FPE

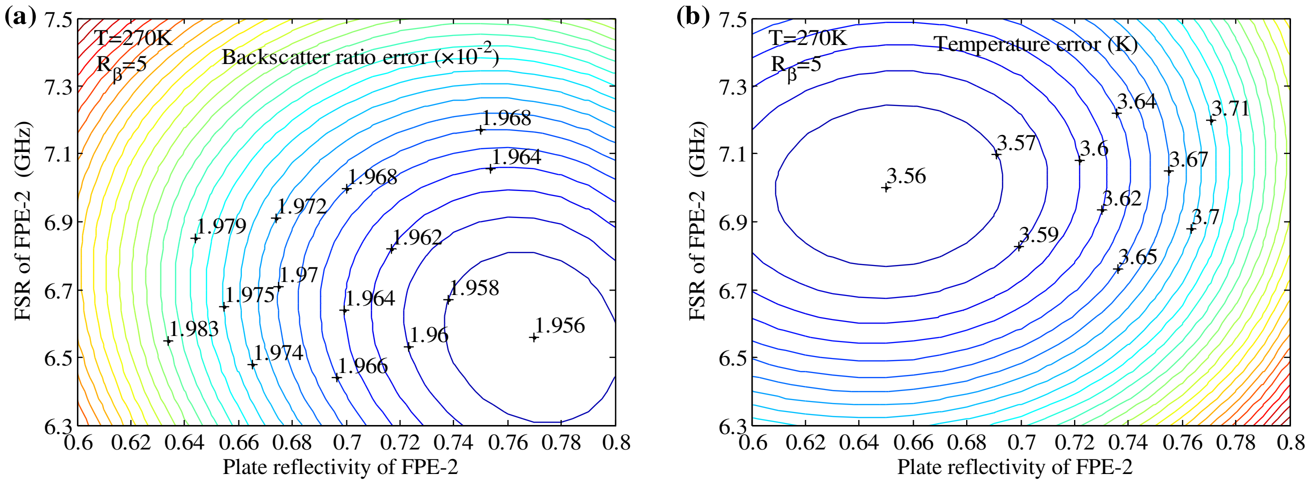

Fig. 6 When $R_\beta = 5$, the measurement error of R_β and T varies with plate reflectivity of FPE-2 and FSR of FPE

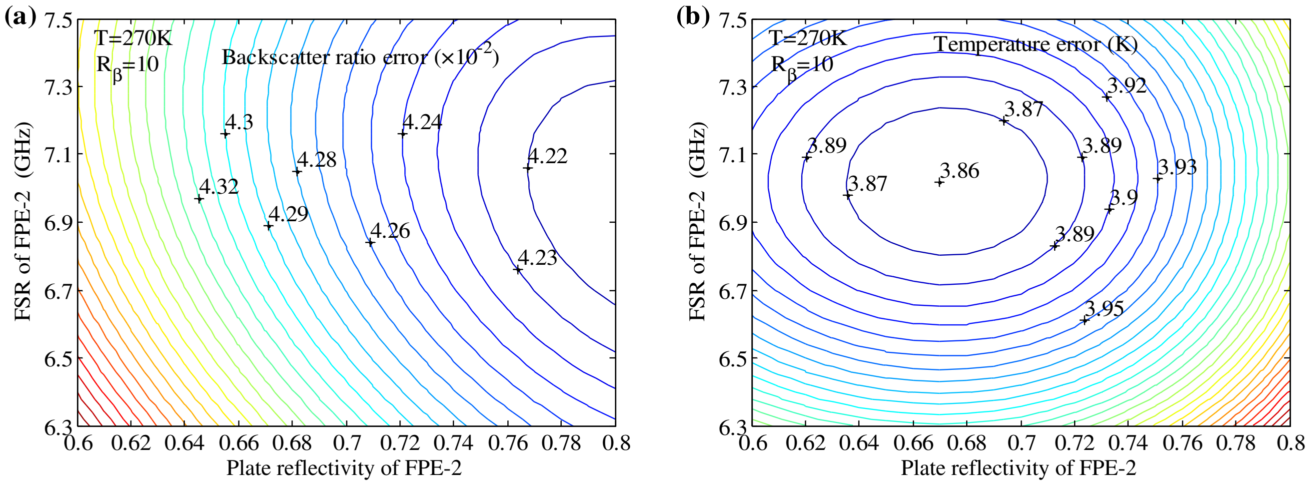

Fig. 7 When $R_\beta = 10$, the measurement error of R_β and T varies with plate reflectivity of FPE-2 and FSR of FPE

Figs. 5a, b, 6a, b and 7a, b, respectively. Looking at those figures, one can see that the optimal parameter values for the backscatter ratio measurement and the temperature measurement are different, and the optimal parameter values for different backscatter ratio are also different. Combining Figs. 5, 6 and 7, one can see that it is not possible to minimize the backscatter ratio error and temperature error simultaneously for different backscatter ratio. After making a compromise between them and mainly considering temperature measurement, the optimal plate reflectivity of FPE-2 is determined to be 0.67 and the optimal FSR of the triple FPE is 7 GHz. Then, it can be further determined that the peak to peak spacing of FPE-1 and FPE-2 is 3.5 GHz.

5 Detection performance simulation

The parameters of the triple FPE optimized in Sect. 4 and other lidar system parameters assumed are summarized in Table 1. Then, the equivalent spectrum broadening $\Delta\nu_d = 123$ MHz and the equivalent linewidth of laser $\delta\nu_e = (4\ln 2)^{1/2}\Delta\nu_a = 220$ MHz. The transmittances of the Mie- and Rayleigh-scattering light at different temperatures (230 and 270 K) being incident on FPE-1, incident on FPE-2 after reflecting by FPE-1, and reflected by FPE-2 after reflecting by FPE-1 are shown in Fig. 8.

The simulated temperature sensitivity of S_T, backscatter ratio sensitivity of S_R, temperature sensitivity of S_R and backscatter ratio sensitivity of S_T for the temperature range of 220–290 K and the backscatter ratio range of 1–10 are shown in Fig. 9a–d. As can be seen from Fig. 9, θ_T is closely

Table 1 Parameters of FPE-based HSRL

	Parameter	Value	Parameter	Value
Transmitter	Wavelength	355 nm	Laser energy/pulse	48 mJ
	Laser linewidth	80 MHz	Laser repetition frequency	20 Hz
Transceiver	Telescope/scanner aperture	25 cm	Field of view	0.1 mrad
	Optical efficiency	> 85%		
Receiver	Etalon free spectral range	7 GHz	Sub-aperture of each FPE	25 mm
	Plate reflectivity of Etalon-1	0.75	FPE-1 and FPE-2 separation	3.5 GHz
	Plate reflectivity of Etalon-2	0.67	FPE-1 and FPE-L separation	0.36 GHz
	Plate reflectivity of Etalon-L	0.75	Loss coefficient of FPE	0.2%
	defect factor of flatness	3 nm	Wedge angle of two plates	0.1 μrad
	Solar filter bandwidth	1 nm	Detector quantum efficiency	21%@355 nm
	Filter peak transmission	> 60%	Detector dark count	100 counts/s

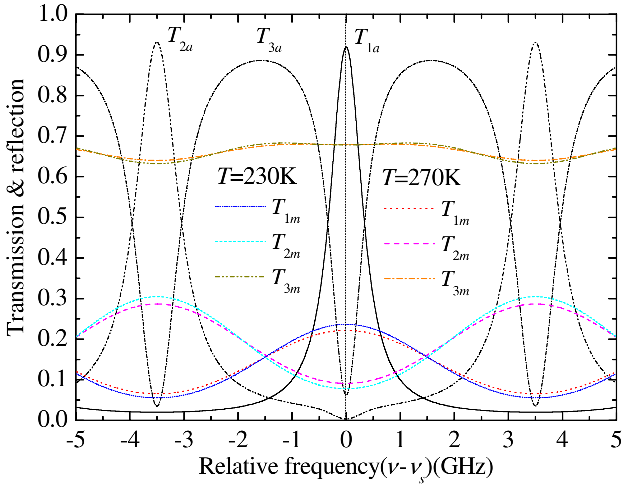

Fig. 8 Mie scattering transmittances of T_{1a}, T_{2a}, T_{3a} and Rayleigh-scattering transmittances of T_{1R}, T_{2R}, and T_{3R}

related to the magnitude of T and R_β, and decreases with increasing T and R_β, its value varies from 0.44 to 0.23%/K as R_β changes from 1 to 10 and T changes from 220 to 290 K. θ_R is almost independent of T and decreases with increasing R_β, its value varies from 4.2 to 7.5% as R_β changes from 1 to 10. θ_{RT} is also mainly affected by R_β and decreases rapidly with increasing R_β, which appears even smaller than θ_T. θ_{TR} is very small compared with θ_R. It is related to both T and R_β, increasing with the increase of T and the decrease of R_β.

Assuming that the number of Rayleigh photoelectrons is 10^5, Fig. 10a, b shows the backscatter ratio and temperature measurement errors of our designed system varying with temperature and backscatter ratio, respectively. As can be seen from Fig. 10a, the backscatter ratio measurement error is almost independent of the temperature, and increases linearly with the increase of backscatter ratio. When R_β = 10, the backscatter ratio measurement error is 4.27–4.41% with temperature range of 220–290 K. As can be seen from Fig. 10b, the temperature measurement error increases with increasing backscatter ratio and temperature. When R_β = 10 and T = 290 K, the temperature measurement error is 4.1 K. For comparison, Fig. 11a, b shows the backscatter ratio and temperature measurement errors of the lidar system proposed by Hua et al. in [23, 24] (denoted by $\varepsilon_{\mathrm{Rh}}$ and $\varepsilon_{\mathrm{Th}}$) varying with temperature and backscatter ratio, respectively. In Fig. 11b, it is assumed when $R_\beta > 2$, the Mie correction method described in Ref. [24] should be adopted to eliminate the temperature offset caused by the residual Mie signal in the two temperature measurement channels. It can be clearly seen that the backscatter ratio and temperature measurement errors shown in Fig. 11 are obviously greater than those shown in Fig. 10. Figure 12a, b shows the ratio of backscatter ratio measurement errors and the ratio of temperature measurement errors obtained by the above two different systems varying with temperature and backscatter ratio, respectively. It can be seen from Fig. 12a, b that under the condition of the same number of received photoelectrons, the backscatter ratio and temperature measurement accuracies of our proposed lidar system are 4.16–22.58 times and 2.07–2.76 times, respectively, that of the system proposed by Hua et al. with temperature range of 220–290 K and backscatter ratio range of 1–10.

The daytime sky background brightness is taken as 0.3 W Sr^{-1} m^{-2} nm^{-1}@355 nm, which is used to simulate the solar background noise; the lidar ratio is taken as 50. Using the system parameters listed in Table 1, the mid-latitude summer model of 1976 US standard atmosphere and the aerosol model of scaling factors in clear weather [41], the detection performance of the lidar system was simulated. With 1-min integration time and 30-m range resolution, the simulated measurement error profiles of temperature and backscatter ratio at the height of 0–12 km are shown in Fig. 13a, b, respectively. As can be seen from Fig. 13a, b, the temperature measurement error is less than 2 K at 8 km and less than 4 K at 12 km; the backscatter ratio measurement error is less than 0.17% at 8 km and less than 0.39% at 12 km. One can also find that the difference in temperature

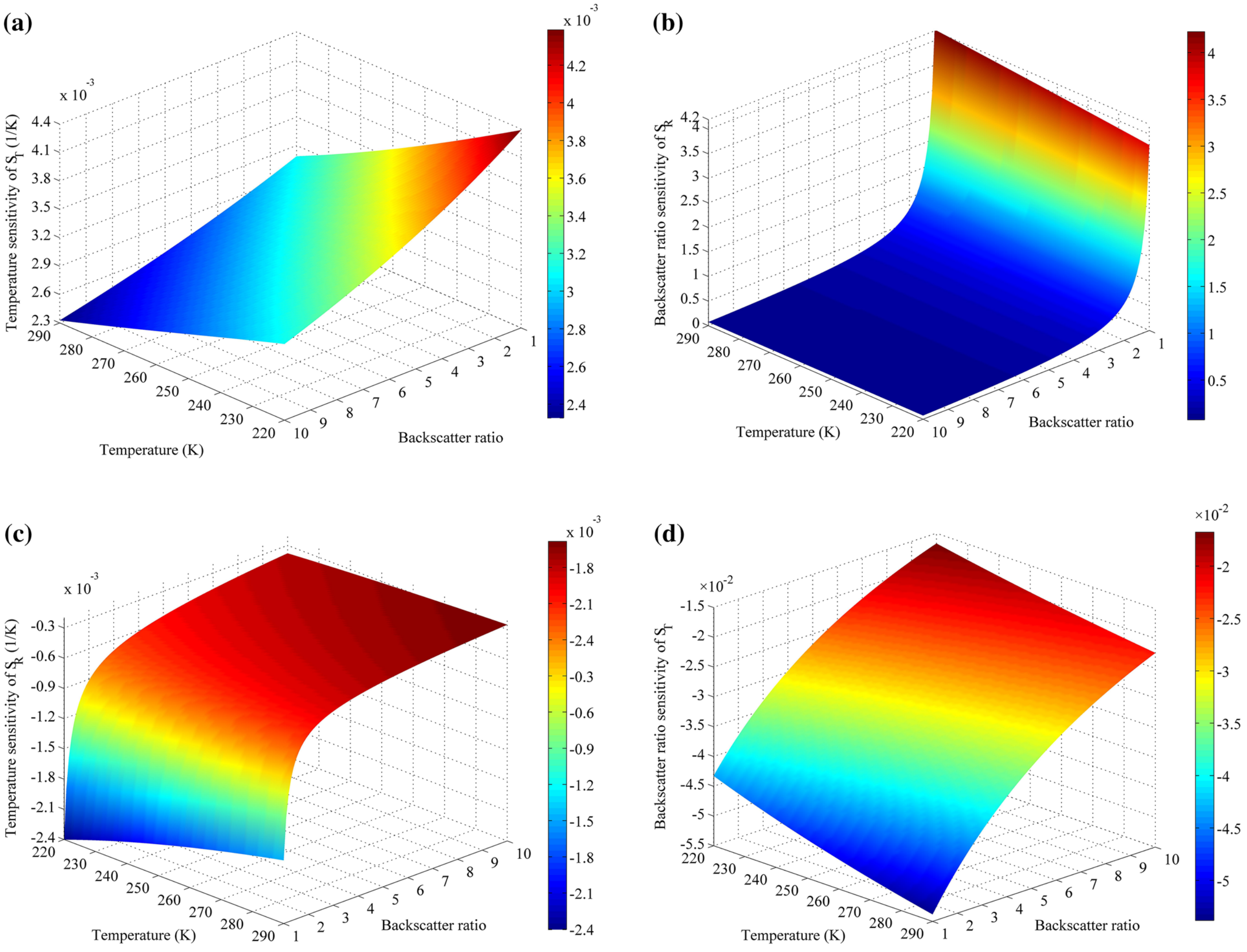

Fig. 9 Temperature sensitivity and backscatter ratio sensitivity

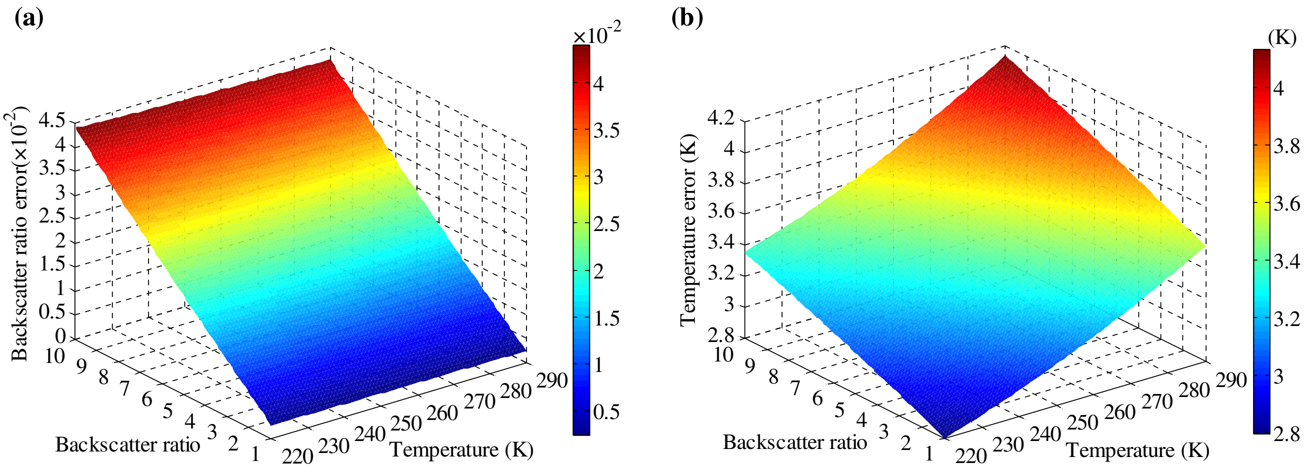

Fig. 10 Measurement errors of backscatter ratio and temperature vary with temperature and backscatter ratio using our designed system

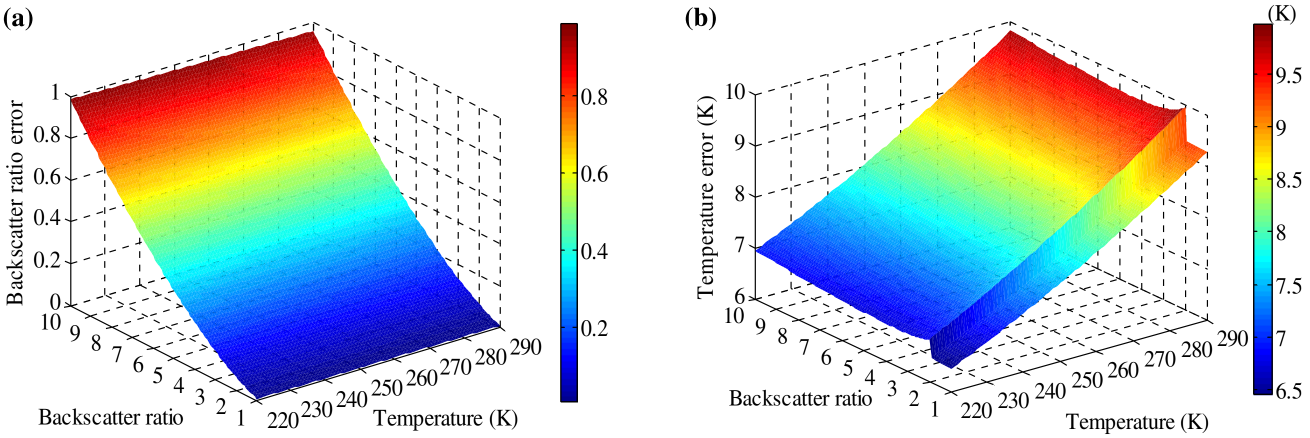

Fig. 11 Measurement errors of backscatter ratio and temperature vary with temperature and backscatter ratio using the lidar system proposed by Hua et al.

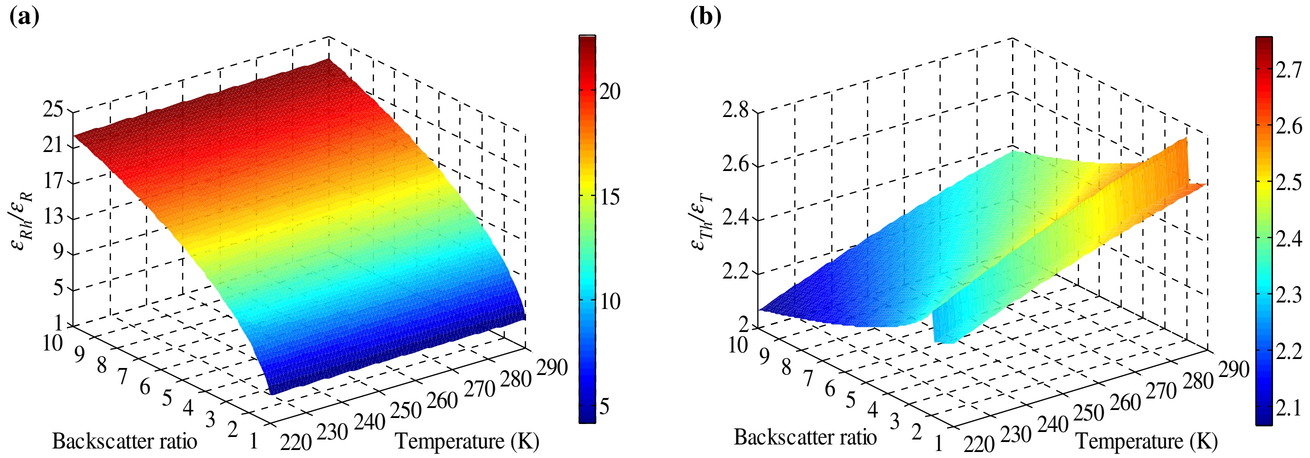

Fig. 12 The ratio of backscatter ratio measurement errors and the ratio of temperature measurement errors obtained by the two different systems varying with temperature and backscatter ratio

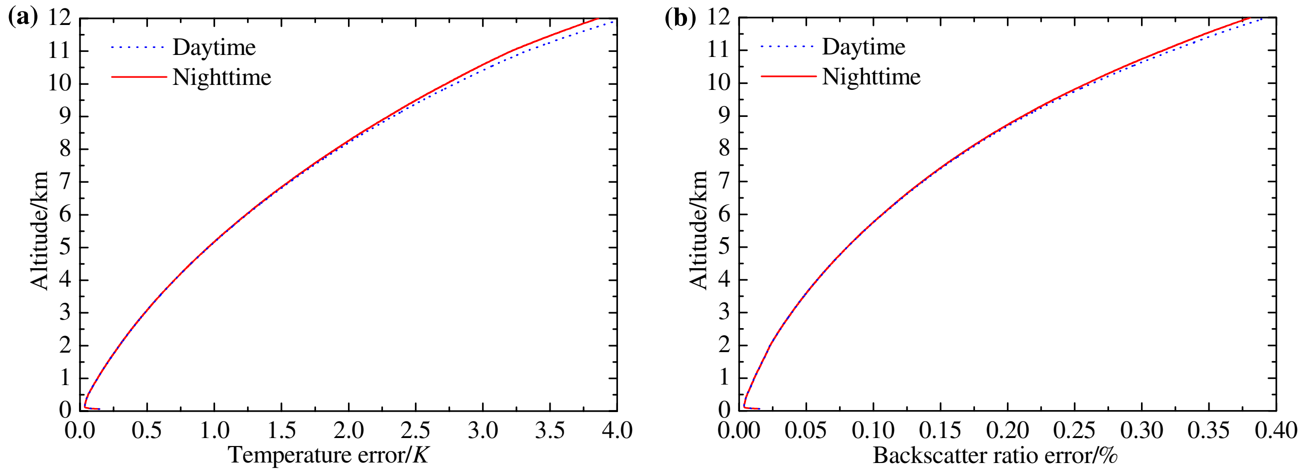

Fig. 13 Profiles of temperature and backscatter ratio measurement errors by simulation

and backscatter ratio measurements between daytime and nighttime is not significant, especially at low altitude. There are three main reasons for this. First, the same atmospheric model is used during daytime and nighttime simulations since there is no separate atmospheric model for daytime and nighttime. Second, our system uses optical polarization technology, narrow band filter and small receiving field of view of the telescope, making it inherently capable of suppressing noise. Third, our system uses a laser with high single pulse energy and low repetition rate. Compared with a laser with low single pulse energy and high repetition rate, the integration time required for obtaining the same total emission energy is shorter, which can effectively reduce the noise entry.

6 The influence of Mie signal contamination and vertical wind speed

The uncertainty of response function due to Mie signal contamination can be derived from Eq. (9) as

$$\frac{\delta S_T}{S_T} = \left(\sum_{j=2,3} \frac{1}{\left[(R_\beta - 1)^{-1} r_j^{-1} + 1\right]^2} \right)^{1/2} \frac{\delta R_\beta}{R_\beta - 1}, \tag{14}$$

where $r_j = T_{ja}/T_{jm}$ is the relative Mie rejection factor of channel-j. Then, the temperature deviation caused by the uncertainty of response function will be as

$$\delta T = \frac{\delta S_T}{S_T} \frac{1}{\theta_T}. \tag{15}$$

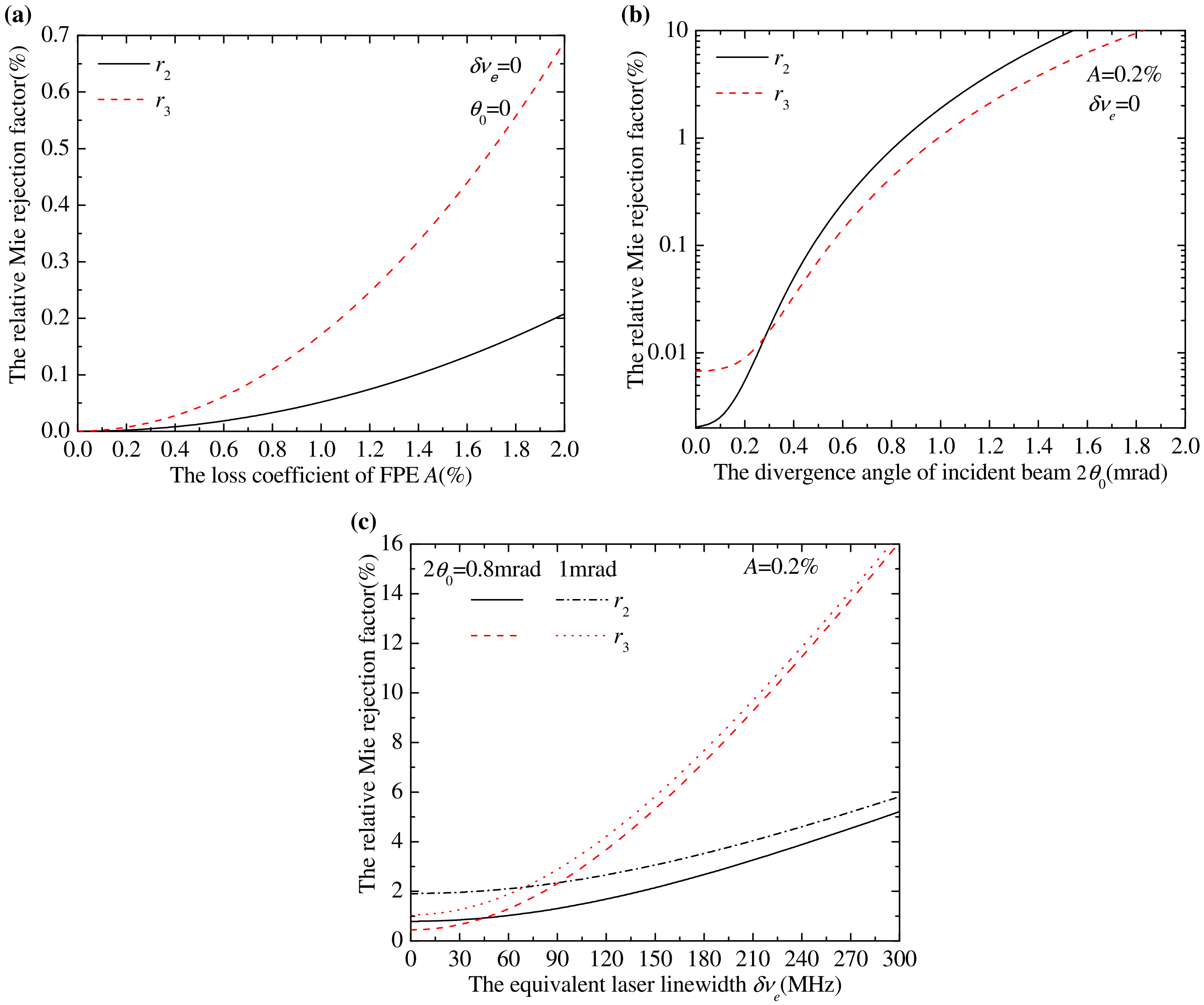

Fig. 14 The relationship between r_2 and r_3, and A, θ_0 and $\delta\nu_e$, respectively

It can be seen clearly that the temperature deviation is closely related to the relative Mie rejection factors of channel-2 and channel-3. Using the Eqs. (4–6), the relative Mie rejection factor of channel-*j* can be simulated. The plate reflectivities of FPE-1 and FPE-2, the FSR of the triple FPE and the peak to peak spacing of FPE-1 and FPE-2, respectively, take the optimized values in Sect. 4. The temperature is set to 270 K. Then, the relative Mie rejection factors are only related to the loss coefficient of FPE, the divergence angle of incident beam and the equivalent linewidth of laser. The effects of surface defects and non-parallelism of FPE are equivalent to broadening the linewidth of emission light source. To take these factors into consideration, the linewidth we refer to here is the equivalent linewidth of outgoing laser that includes the widening of these factors [36]. Figure 14a–c shows the relationship between the relative Mie rejection factors of channel-2 and -3 and them with vertical wind speed of zero. From Fig. 14a, one can see that the relative Mie rejection factors increase slowly with increasing the loss coefficient of FPE A. If A is below 0.3%, its impact can be ignored. We choose the value of A to be 0.2%. From Fig. 14b, one can see that the relative Mie rejection factors increase rapidly with increasing the divergence angle of incident beam $2\theta_0$. Without considering the equivalent laser linewidth, to make r_2 and r_3 both less than 2%, $2\theta_0$ must be less than 1 mrad. If $2\theta_0$ is 0.8 mrad, r_2 and r_3 would be less than 0.8 and 0.4%, respectively. It can be seen from Fig. 14c that the relative Mie rejection factors increase with increasing the equivalent laser linewidth $\delta\nu_e$, r_2 increases slowly and r_3 increases rapidly. When A is 0.2%, $2\theta_0$ is 1 mrad, and $\delta\nu_e$ takes 220 MHz, r_2 and r_3 would be 4.2 and 10.4%, respectively. With backscatter ratio of 10 and temperature of 270 K, the backscatter ratio measurement error δR_β is about 4.3% for 10^5 Rayleigh photoelectrons as shown in Fig. 10a and θ_T is about 0.26%/K as shown in Fig. 9a. In this case, the temperature deviation due to Mie signal contamination would be about 1 K. If we take $A = 0.2\%$, $2\theta_0 = 0.8$ mrad, and $\delta\nu_e = 150$ MHz, r_2 and r_3 would be 2.1 and 5.3%, then the temperature deviation would be 0.65 K. It is important to note that in our proposed system, the backscatter ratio and temperature are simultaneously measured, and Mie correction is automatically included in data processing. Therefore, the temperature error represented by Eq. (11) already contains the temperature deviation due to Mie signal contamination.

Besides, the vertical wind speed will still cause the measurement bias of backscatter ratio and temperature. Fortunately, the vertical wind speed is usually very small as mentioned in Sect. 4, not more than 1 m/s. Figure 15a, b shows the measurement bias of backscatter ratio and temperature vary with vertical wind speed for different backscatter ratio. From Fig. 15, one can see that the backscatter ratio and temperature measurement bias increase as the backscatter ratio and vertical wind speed increase; the backscatter ratio measurement bias is from 0 to -2.2% and the temperature measurement bias is 0–0.5 K with backscatter ratio range of 1–10 assuming a vertical wind speed of 1 m/s.

7 Conclusions

This paper presents a FPE-based UV HSRL technique for simultaneous measurement of tropospheric temperature and aerosols. The main innovations and advantages of this technique are as follows: the Rayleigh scattering signal is directly separated from the total backscattering signal for

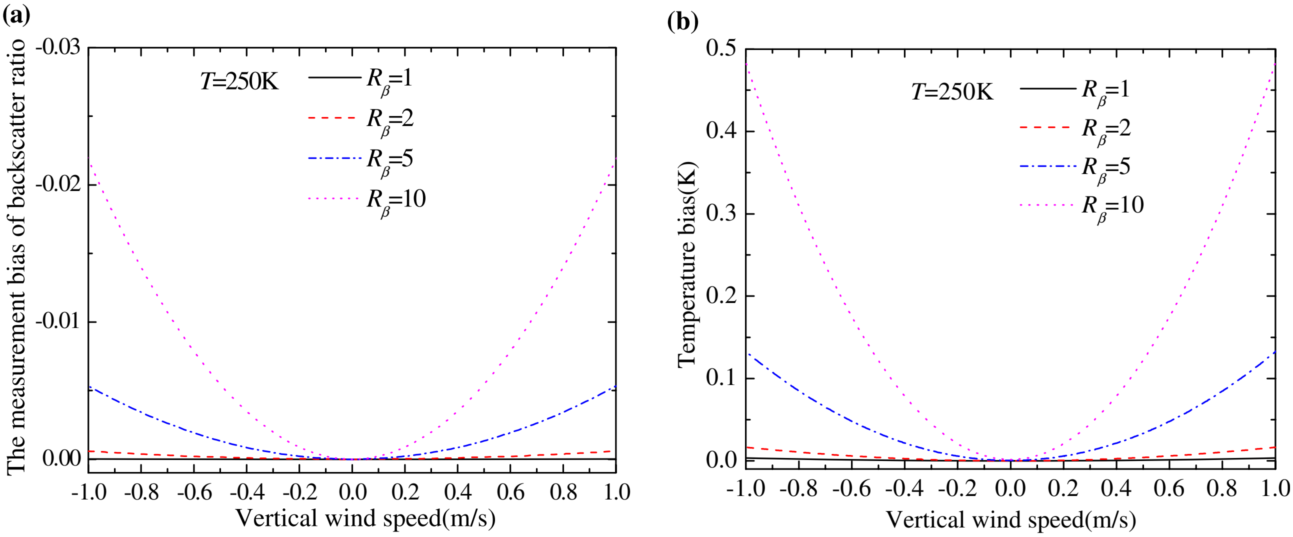

Fig. 15 Measurement bias of backscatter ratio and temperature vs vertical wind speed for different backscatter ratio

temperature detection by hardware; the polarization isolation method is used to make the backscattering signal highly efficient and the background effectively suppressed; the SNR of temperature detection is effectively improved using the adjacent two order spectrums of the FPE to simultaneously measure the two wings of the Rayleigh scattering spectrum; the backscatter ratio and temperature are simultaneously measured, then Mie correction is automatically included in data processing for temperature measurement. The overall design of the lidar system is carried out, and the triple FPE parameters used in the system are optimized in detail. Using the set system parameters and the optimized parameters of the triple FPE, the simulation results show that the system can achieve high-accuracy measurement of the temperature and backscatter ratio at height of 0–12 km. The influence of Mie signal contamination on temperature measurement is analyzed. It mainly depends on the relative Mie rejection factors of the two channels for temperature measurement, which are related to the loss coefficient of FPE, the divergence angle of incident beam and the equivalent linewidth of outgoing laser. By choosing reasonable system parameter values, the temperature deviation caused by Mie signal contamination can be greatly reduced. The influence of a small vertical wind speed on temperature and aerosol measurements is also discussed. The measurement bias of backscatter ratio and temperature is from 0 to − 2.2% and 0–0.5 K, respectively, with backscatter ratio range of 1–10 and vertical wind speed of 1 m/s. The designed lidar system has good detection performance, and the system will promote a better study on atmospheric thermodynamics and kinetics after it is built. Furthermore, if the optical path of the receiver is modified and the signal transmitted from the aerosol channel etalon (FPE-1) is guided into the locking channel etalon (FPE-L), the proposed lidar system can also be used to measure the wind speed based on Mie signal.

Acknowledgements This work was supported by the Natural Science Foundation of Jiangsu Province, China (BK20161316), the Open Research Fund of Key Laboratory of Atmospheric Composition and Optical Radiation, Chinese Academy of Sciences (2017), the Young Scientists Fund of the National Natural Science Foundation of China (51504214).

References

1. J.D. Klett, Stable analytical inversion solution for processing lidar returns. Appl. Opt. **20**, 211–220 (1981)
2. F.G. Fernald, Analysis of atmospheric lidar observations: some comments. Appl. Opt. **23**, 652–655 (1984)
3. D. Hua, X. Song, Advances in lidar remote sensing techniques. Infrared Laser Eng. **37**, 26–32 (2008)
4. N. Sugimoto, I. Matsui, Z. Liu, A. Shimizu, I. Tamamushi, K. Asai, Observation of aerosols and clouds using a two-wavelength polarization lidar during the Nauru99 experiment. Sea Sky **76**, 93–98 (2000)
5. G. Bo, D. Liu, B. Wang, D. Wu, Z. Zhong, Two-wavelength polarization airborne lidar for observation of aerosol and cloud. Chin. J. Lasers **39**, 203–208 (2012)
6. J.T. Sroga, E.W. Eloranta, S.T. Shipley, F.L. Roesler, P.J. Tryon, High spectral resolution lidar to measure optical scattering properties of atmospheric aerosols. 2: Calibration and data analysis. Appl. Opt. **22**, 3725–3732 (1983)
7. C.Y. She, R.J. Alvarez II, L.M. Caldwell, D.A. Krueger, High-spectral-resolution Rayleigh–Mie lidar measurement of vertical aerosol and atmospheric profiles., Appl. Phys. B **55**, 541–543 (1992)
8. J.E. Kalshoven Jr, C.L. Korb, G.K. Schwemmer, M. Dombrowski, Laser remote sensing of atmospheric temperature by observing resonant absorption of oxygen. Appl. Opt. **20**, 1967–1971 (1981)
9. F.A. Theopold, J. Bösenberg, Differential absorption lidar measurements of atmospheric temperature profiles: theory and experiment. J. Atmos. Ocean. Technol. **10**, 165–179 (1993)
10. V. Wulfmeyer, Ground-based differential absorption lidar for water-vapor and temperature profiling: development and specifications of a high-performance laser transmitter. Appl. Opt. **37**, 3804–3824 (1998)
11. J. Bösenberg, Ground-based differential absorption lidar for water-vapor and temperature profiling: methodology. Appl. Opt. **37**, 3845–3860 (1998)
12. A. Hauchecorne, M.L. Chanin, Density and temperature profiles obtained by lidar between 35 and 70 km. Geophys. Res. Lett. **7**, 565–568 (1980)
13. W.N. Chen, C.C. Tsao, J.B. Nee, Rayleigh lidar temperature measurements in the upper troposphere and lower stratosphere. J. Atmos. Sol. Terr. Phys. **66**, 39–49 (2004)
14. L. Bu, J. Guo, L. Tian, X. Huang, B. Liu, Y. Feng, Rayleigh-Raman lidar used for atmospheric temperature profile measurement. High Power Laser Part. Beams **7**, 1449–1452 (2010)
15. G. Fiocco, G. Beneditti-Machelangeli, K. Maschberger, E. Madonna, Measurement of temperature and aerosol to molecule ratio in the troposphere by optical radar. Nat. Phys. Sci. **229**, 78–79 (1971)
16. B. Witschas, C. Lemmerz, O. Reitebuch, Daytime measurements of atmospheric temperature profiles (2–15 km) by lidar utilizing Rayleigh–Brillouin scattering. Opt. Lett. **39**, 1972–1975 (2014)
17. R.L. Schwiesow, L. Lading, Temperature profiling by Rayleigh scattering lidar. Appl. Opt. **20**, 1972–1979 (1981)
18. H. Shimizu, S.A. Lee, C.Y. She, High spectral resolution lidar system with atomic blocking filters for measuring atmospheric parameters. Appl. Opt. **22**, 1373–1381 (1983)
19. H. Shimizu, K. Nogachi, C.Y. She, Atmospheric temperature measurement by a high spectral resolution lidar. Appl. Opt. **25**, 1460–1466 (1986)
20. C.Y. She, R.J. Alvarez, L.M. Caldwell, D.A. Krueger, High spectral resolution Rayleigh–Mie lidar measurement of aerosol and atmospheric profiles. Opt. Lett. **17**, 541–543 (1992)
21. D.A. Krueger, L.M. Caldwell, R.J. Alvarez II, and C.Y. She, Self-consistent method for determining vertical profiles of aerosol and atmospheric properties using a high spectral resolution Rayleigh–Mie lidar. J. Atmos. Ocean. Technol. **10**, 533–545 (1993)
22. C.A. Tepley, S.I. Sargoytchev, R. Rojas, The Doppler Rayleigh lidar system at Arecibo. IEEE Trans. Geosci. Remote Sens. **31**, 36–47 (1993)
23. D. Hua, T. Kobayashi, Ultraviolet Rayleigh–Mie lidar by use of a multicavity Fabry–Perot filter for accurate temperature profiling of the troposphere. Appl. Opt. **44**, 6474–6478 (2005)
24. D. Hua, M. Uchida, T. Kobayashi, UV Rayleigh–Mie lidar with Mie scattering correction by Fabry–Perot etalon for temperature profiling of the troposphere. Appl. Opt. **44**, 1305–1314 (2005)
25. H. Xia, X. Dou, M. Shangguan, R. Zhao, D. Sun, C. Wang, J. Qiu, Z. Shu, X. Xue, Y. Han, Y. Han, Stratospheric temperature

measurement with scanning Fabry–Perot interferometer for wind retrieval from mobile Rayleigh Doppler lidar. Opt. Express **22**, 21775–21789 (2014)

26. Z.S. Liu, D.C. Bi, X.Q. Song, J.B. Xia, R.Z. Li, Z.J. Wang, C.Y. She, Iodine-filter-based high spectral resolution lidar for atmospheric temperature measurements. Opt. Lett. **34**, 2712–2714 (2009)
27. R.J. Alvarez, Measurement of tropospheric temperature and aerosol extinction using high spectral resolution lidar. Ph.D. Thesis Colorado State Univ., Fort Collins, (1991)
28. G. Vaughan, D.P. Wareing, S.J. Pepler, L. Thomas, V. Mitev, Atmospheric temperature measurements made by rotational Raman scattering. Appl. Opt. **32**, 2758–2764 (1993)
29. N. Nedeljkovic, A. Hauchecorne, M.L. Chanin, Rotational Raman lidar to measure the atmospheric temperature from the ground to 30 km. IEEE Trans. Geosci. Remote Sens. **31**, 90–101 (1993)
30. A. Behrendt, J. Reichardt, Atmospheric temperature profiling in the presence of clouds with a pure rotational Raman lidar by use of an interference filter based polychromator. Appl. Opt. **39**, 1372–1378 (2000)
31. A. Behrendt, T. Nakamura, M. Onishi, R. Baumgrat, T. Tsuda, Combined Raman lidar for the measurement of atmospheric temperature, water vapor, particle extinction coefficient, and particle backscatter coefficient. Appl. Opt. **41**, 7657–7666 (2002)
32. Y. Arshinov, S. Bobrovnikov, I. Serikov, A. Ansmann, U. Wandinger, D. Althausen, I. Mattis, D. Müller, Daytime operation of a pure rotational Raman lidar by use of a Fabry–Perot interferometer. Appl. Opt. **44**, 3593–3603 (2005)
33. S. Wang, J. Su, P. Zhao, K. Cao, S. Hu, H. Wei, K. Tan, H. Hu, A pure rotational Raman-lidar based on three-stage Fabry–Perot etalons for monitoring atmospheric temperature. Acta Phys. Sin. **57**, 3941–3946 (2008)
34. G. Tenti, C.D. Boley, R.C. Desai, On the kinetic model description of Rayleigh–Brillouin scattering from molecular gases. Can. J. Phys. **52**, 285–290 (1974)
35. M.J. Mcgill, J.D. Spinhirne, Comparison of two direct-detection Doppler lidar techniques. Opt. Eng. **37**, 2675–2686 (1998)
36. F. Shen, Y. Xia, A. Yu, C. Liu, Transmission spectral characteristics of F–P interferometer under multi-factors. Infrared Laser Eng **6**, 1800–1805 (2015)
37. G.J. Sloggett, Fringe broadening in Fabry–Perot interferometers. Appl. Opt. **23**, 2427–2432 (1984)
38. J.A. Mckay, D.J. Rees, High-performance Fabry–Perot etalon mount for spaceflight. Opt. Eng. **39**, 315–319 (2000)
39. X. Xu, N. Weng, L. Xiao, G. Sun, Detecting the vertical velocity in the atmosphere boundary layer in Hefei using Sodar. J. Atmos. Environ. Opt. **5**, 101–104 (2006)
40. A. Souprayen, A. Garnier, A. Hertzog, J. Hauchecorne, Porteneuve, Rayleigh–Mie Doppler wind lidar for atmospheric measurements. I. Instrumental setup, validation, and first climatological results. Appl. Opt. **38**, 2410–2421 (1999)
41. R.A. McClatchey, A.P. D'Agati, Atmospheric transmission of laser radiation. AFGL Report, No. TR-78-0029, USA (1978) p. 24